AIAA JOURNAL
Vol. 42, No. 12, December 2004

Large-Eddy Simulation of Shock-Turbulence Interaction

R. von Kaenel* and L. Kleiser†
ETH Zürich, CH-8092 Zurich, Switzerland
N. A. Adams‡
Technical University of Dresden, D-01062 Dresden, Germany
and
J. B. Vos§
CFS Engineering SA, CH-1015 Lausanne, Switzerland

The approximate deconvolution model (ADM) for large-eddy simulation (LES) is adapted for use with a central fourth-order finite volume (Jameson-type) scheme widely applied for aerodynamics calculations of industrial interest. With ADM, an approximation of the unfiltered solution is obtained by repeated filtering, and given a good approximation of the unfiltered solution the nonlinear terms of the filtered Navier–Stokes equation are computed directly. The effect of scales not represented on the numerical grid is modeled by a relaxation regularization involving a secondary filter operation and a relaxation parameter. The supersonic turbulent boundary layer along a compression ramp at a freestream Mach number of $M = 3$ and a Reynolds number (based on free-stream quantities and the mean momentum thickness at inflow) of $Re_\theta = 1685$ is computed to evaluate the ability of ADM to represent discontinuities and turbulent flow regions. It was observed that a unified modeling of discontinuities and turbulence required a local adaptation of the secondary filter used for the relaxation regularization. The LES results are compared with corresponding filtered direct-numerical-simulation (DNS) data. Very good agreement between the filtered DNS and the LES is observed for the mean, fluctuating, and averaged wall quantities.

Nomenclature

C_f	=	skin-friction coefficient
c_p, c_v	=	specific heat coefficients at constant pressure, volume
E	=	total energy
$\boldsymbol{F}$	=	flux vector
$\mathbb{F}$	=	flux tensor
F_{ij}^k	=	kth component of the flux vector through the jth cell face of the ith cell
$\boldsymbol{f}_{\text{inv}}$, $\boldsymbol{f}_v$	=	vector of inviscid, viscous flux in x_1 direction
G_1, G_2	=	primary, secondary filter kernel
$\boldsymbol{g}_{\text{inv}}$, $\boldsymbol{g}_v$	=	vector of inviscid, viscous flux in x_2 direction
H_k	=	structure function
h	=	computational-space grid interval
$\boldsymbol{h}_{\text{inv}}$, $\boldsymbol{h}_v$	=	vector of inviscid, viscous flux in x_3 direction
L_i	=	length in the ith direction
M	=	Mach number
N	=	deconvolution order
N_i	=	number of cells in each coordinate direction
$\boldsymbol{n}$, n_i	=	normal vector, components
n_{faces}	=	number of faces of a control volume
Pr	=	Prandtl number
p	=	pressure
q_i	=	heat flux caused by conduction
Re	=	computational Reynolds number
Re_θ	=	Reynolds number based on the momentum thickness of the boundary layer
S	=	cell surface
$\boldsymbol{S}$	=	surface vector
s	=	Sutherland's law constant
T	=	temperature
t	=	time
$\boldsymbol{U}$	=	state vector of conservative variables
$\boldsymbol{U}_i$	=	state vector of conservative variables averaged over the ith cell
$\boldsymbol{u}$,u_i	=	velocity vector, components
V	=	control volume
x_i	=	coordinate directions
α_i	=	filter coefficients
β	=	compression ramp angle
γ	=	c_p/c_v
Δ	=	interval
δ_1	=	displacement thickness of the boundary layer
μ	=	dynamic viscosity
ν_l,ν_r	=	left, right filter stencil bound
ξ_i	=	coordinate directions in computational space
ρ	=	density
τ	=	shear stress
τ_{ij}	=	components of the shear-stress tensor
χ	=	relaxation coefficient
ω	=	wave number
ω_c	=	filter cutoff wave number
ω_n	=	numerical (Nyquist) cutoff wave number
$*$	=	convolution operator
$\langle\cdot\rangle$	=	averaged quantities

Subscripts

inv	=	inviscid quantity
VD	=	van Driest transformed quantity
v	=	viscous quantity
w	=	wall quantity
∞	=	free-stream quantity

Superscripts

c	=	contravariant quantity
$*$	=	dimensional quantity
-	=	filtered quantity

Presented as Paper 2003-3962 at the 16th Computational Fluid Dynamics Conference, Orlando, FL, 23–26 June 2003; received 24 October 2003; revision received 13 May 2004; accepted for publication 25 May 2004.

*Assistant, Institute of Fluid Dynamics, Sonneggstrasse 3; vonkaenel@ifd.mavt.ethz.ch.
†Professor, Institute of Fluid Dynamics, Sonneggstrasse 3. Member AIAA.
‡Professor, Institute of Fluid Mechanics, Ġeorge-Bähr Str. 3c.
§Senior Research Scientist, PSE-B.

$\star$ = deconvolved quantity
$\breve{}\star$ = computed with deconvolved quantities
$+$ = quantity in wall units
$\sim$ = Favre-averaged quantity
$'$ = fluctuating quantity
$''$ = Favre fluctuations

I. Introduction

ACCURATE computations of shock-boundary-layer interaction are needed in many aerospace and aeronautical applications to predict, for example, flows around transonic airfoils, supersonic air intakes, or deflected control surfaces of vehicles at transonic or supersonic speed. To achieve an optimal and safe design of these high-speed vehicles or vehicle components, critical quantities such as skin-friction, heat-transfer rates, fluctuating pressure, and thermal loads have to be known precisely.

Experimental research into shock-boundary-layer interaction started in the mid-1940s with the work of Ackeret et al.[1] and has shown a constant interest since then (see Dolling[2]). Numerical simulations of supersonic shock-boundary-layer interaction using Reynolds-averaged Navier–Stokes equations (RANS) methods are being made since the end of the 1970s. For example, Settles et al.[3] compared experimental data with computations of the flow over a compression corner at high Reynolds number and observed that the RANS turbulence models at that time were unable to predict accurately the skin friction, the location of the flow separation and reattachment, the surface pressure, and the heat transfer for strong shock-turbulence interaction. More recently, Knight and Degrez[4] made an evaluation on how well widely used turbulence models could predict these complex flows. Their conclusions were also rather disappointing for flows with significant separation, for which quantities critical for the design of high-speed vehicles, such as the skin-friction and the heat-transfer rates, could not be predicted with confidence, whereas other parameters such as the fluctuating pressure and thermal loads could not be computed at all with RANS. Knight and Degrez[4] attributed the poor results mainly to two causes. First, RANS calculations do not model flowfield unsteadiness. This can alter mean quantities because low-frequency unsteady phenomena are expected to influence these quantities. Second, turbulent eddy-viscosity models characterize the turbulence using a single length scale, which is incorrect in separated flows. Other uncertainties in RANS simulations come from three-dimensional flow structures and compressibility effects.

Because of the limitations of RANS, large-eddy simulation (LES) is becoming more and more popular to simulate numerically these kind of flows. In LES, the large eddies are resolved, which correspond to large scales, while the effect of the small eddies is modeled. The separation between large and small scales is obtained by application of a spatial filter to the Navier–Stokes equations yielding the filtered Navier–Stokes equations with corresponding filtered variables. Unlike RANS, in which only the mean flow is solved and the entire turbulence is modeled, LES models only the small-scale turbulence, and the filtered variables contain thus much more information than the RANS variables. LES has therefore the potential to become the preferred predictive approach for complex flows although today it still cannot be used straightforwardly. Challenges for LES of shock-turbulence interaction are identified on two levels: first on the numerical level with the use of accurate, nondissipative, and stable schemes and second on the level of LES with the requirement of a subgrid-scale model capable of providing a unified modeling of the turbulent and nonturbulent subgrid scales (shocks).

The development of numerical schemes for flows with discontinuities started well before one was thinking about using LES for this kind of flows. Lax and Wendroff[5] and Godunov[6] already worked on this difficult task in the end of the 1950s and stated that a numerical scheme has to be conservative and monotone in order to converge in a nonoscillatory way to the correct entropy solution. Unfortunately, as demonstrated by Godunov, linear monotone methods are at most first-order accurate, giving poor accuracy in smooth regions of the flow and smeared representation of discontinuities. Higher-order methods give much better accuracy on smooth solutions but fail near discontinuities, where oscillations are generated. The idea with high-resolution methods is to combine the advantages of the low- and high-order discretization properties. This can only be achieved by adding nonlinear terms to the second- or higher-order discretized conservation law leading to schemes augmented with artificial numerical dissipation terms, total-variation-diminishing schemes or nonoscillatory [essentially nonoscillatory (ENO), weighted essentially nonoscillatory (WENO)] schemes, all of them being commonly referred to as shock-capturing schemes.[7]

One open question with shock-capturing schemes is whether they qualify for LES because the dissipation introduced by the additional nonlinear terms can mask the effect of subgrid-scale models. This fundamental question was addressed by Garnier et al.,[8] who investigated the interaction between some widely used shock-capturing schemes and the Smagorinsky[9] and the dynamic model of Germano et al.[10] They came to the conclusion that in many cases the intrinsic numerical dissipation of the shock-capturing schemes masks the effect of the subgrid-scale model. The idea of using the artificial dissipation of a numerical scheme in a turbulence modeling prospect was first proposed by Boris et al.,[11] who argued that it could mimic the effect of a subgrid-scale model. This approach, known as MILES (monotonically integrated LES), was investigated lately in more detail by Fureby and Grinstein[12] and Garnier et al.[8] and has shown to give rather good results for free shear flow and forced homogeneous turbulence at higher Reynolds number, whereas it does not perform so well for decaying turbulence or at lower Reynolds number. Recently, good results were also obtained for wall-bounded flows.[13]

Few studies have been undertaken so far to investigate the influence of subgrid-scale models on shocks. Subgrid-scale models have been developed to account for the energy transfer from resolved scales to nonrepresented scales and are often based on assumptions of turbulence isotropy or scale similarity that are not valid in the presence of a discontinuity. A challenge for the subgrid-scale model is to provide a unified modeling of the turbulent and nonturbulent subgrid scales (shocks).

Without any special shock treatment, Stolz et al.[14] obtained very good results of LES with the approximate deconvolution model (ADM) using a sixth-order compact finite difference discretization for the same flow configuration as considered herein, that is, the Mach 3 compression ramp. Recently, Adams and Stolz[15] investigated more in depth if ADM was able to provide a unified treatment of flow discontinuities and turbulent subgrid scales. Using a sixth-order compact finite difference scheme, they varied the order of the filter used for the relaxation regularization and performed tests for shock solutions of the Burgers and Euler equations.

Garnier et al.[16] studied shock-boundary-layer interaction using LES. They selected the two-dimensional interaction of an oblique shock on a flat-plate boundary layer to assess the ability of the mixed-scale model[17] to cope with complex flows. The numerical scheme employed a combination of a fourth-order centered base scheme with a fifth-order accurate WENO filter. The results were compared with experimental data and showed good agreement except for cross-term fluctuations that appeared underestimated. In relation with the MILES approach, they also performed computations without an explicit subgrid-scale model to evaluate the effect of the subgrid-scale model and noted that, except for an improved prediction of the skin-friction coefficient, its effect was globally rather small compared to the intrinsic dissipation of the numerical method.

Identical to the flow configuration studied in this paper, Rizetta and Visbal[18] performed simulations of the flow over a supersonic compression ramp. They employed a sixth-order compact finite difference scheme in conjunction with a tenth-order nondispersive filter, which is periodically applied to the solution. Because of the excessive diffusion of the shock caused by the repeated filtering, they replaced the compact differencing of the convective derivatives and filter operation by a third-order Roe upwind-biased method locally in regions of shock waves. The subgrid-scale terms were accounted for by the dynamic Smagorinsky model. The results of the numerical simulations were compared with the direct-numerical-simulation (DNS) data of Adams[19] and experimental data, the latter

were, however, obtained for significantly different flow parameters (Reynolds number two orders of magnitude higher) and a different geometric configuration. (The sidewall end plates in the experiment were not modeled in the numerical simulation.) As a result, the agreement between computed results and experimental data was rather qualitative than quantitative. Some discrepancies with the DNS results of Adams were also observed and have mainly been attributed to different inflow conditions.

Stolz and Adams[20] developed a subgrid-scale model based on approximate deconvolution and demonstrated excellent performance of the model for a number of canonical flow configurations, including incompressible wall-bounded flows[21] and shock-turbulence interaction in a boundary layer.[14] More recently, Rembold et al.[22] also obtained very good results with ADM for the compressible rectangular jet. For flows at higher Reynolds numbers, a relaxation regularization is employed to represent the resolved-scale/nonrepresented-scale interaction. Computations were mainly performed with high-order (sixth-order) finite difference and spectral schemes.

In previous works,[23,24] we addressed the extension of ADM to the finite volume method, its implementation in a numerical code (NSMB[25]), which is being used in standard computational-fluid-dynamics design tasks of the aerospace industry, and a validation of the method for the turbulent compressible channel flow. Following the good results obtained for the channel flow, the objective of the present investigation is to evaluate ADM for a more complex flow, that is, shock-turbulence interaction on a compression ramp.

The governing equations are introduced first, followed by the presentation of the filtering, deconvolution, and relaxation procedure extended to the finite volume method. Next, we outline the parameters of the simulation and summarize the numerical method. The benefit of the local adaptation to the flow of the secondary filter is assessed, and finally the results of LES with ADM are compared with the filtered DNS data of Adams.[19]

II. Governing Equations

The flow is described by the compressible Navier–Stokes equations and expressed in conservative form for the three space coordinates x_1, x_2, x_3 as

$$\frac{\partial}{\partial t}\boldsymbol{U}+\frac{\partial}{\partial x_1}(\boldsymbol{f}_{\text{inv}}-\boldsymbol{f}_v)+\frac{\partial}{\partial x_2}(\boldsymbol{g}_{\text{inv}}-\boldsymbol{g}_v)+\frac{\partial}{\partial x_3}(\boldsymbol{h}_{\text{inv}}-\boldsymbol{h}_v)=0 \quad (1)$$

An ideal gas is considered, and the variables are nondimensionalized with the freestream velocity u^*_∞ ($*$ quantities are dimensional), density ρ^*_∞, temperature T^*_∞, and displacement thickness δ^*_1 of the mean boundary layer at inflow. The time t is nondimensionalized with δ^*_1/u^*_∞. The state vector of the conservative variables is given by $\boldsymbol{U}=(\rho, \rho u_1, \rho u_2, \rho u_3, E)$, where the inviscid fluxes are defined as

$$\boldsymbol{f}_{\text{inv}}=\begin{pmatrix}\rho u_1\\ \rho u_1^2+p\\ \rho u_1u_2\\ \rho u_1u_3\\ u_1(E+p)\end{pmatrix},\qquad \boldsymbol{g}_{\text{inv}}=\begin{pmatrix}\rho u_2\\ \rho u_2u_1\\ \rho u_2^2+p\\ \rho u_2u_3\\ u_2(E+p)\end{pmatrix}$$

$$\boldsymbol{h}_{\text{inv}}=\begin{pmatrix}\rho u_3\\ \rho u_3u_1\\ \rho u_3u_2\\ \rho u_3^2+p\\ u_3(E+p)\end{pmatrix} \quad (2)$$

and the viscous fluxes are

$$\boldsymbol{f}_v=\begin{pmatrix}0\\ \tau_{11}\\ \tau_{12}\\ \tau_{13}\\ (\tau\boldsymbol{u})_1-q_1\end{pmatrix},\qquad \boldsymbol{g}_v=\begin{pmatrix}0\\ \tau_{21}\\ \tau_{22}\\ \tau_{23}\\ (\tau\boldsymbol{u})_2-q_2\end{pmatrix}$$

$$\boldsymbol{h}_v=\begin{pmatrix}0\\ \tau_{31}\\ \tau_{32}\\ \tau_{33}\\ (\tau\boldsymbol{u})_3-q_3\end{pmatrix} \quad (3)$$

The shear-stress tensor τ_{ij} is given by (the summation rule applies and $\delta_{ij}=1$ for $i=j$ and 0 otherwise, $i, j=1, 2, 3$)

$$\tau_{ij}=\frac{\mu(T)}{Re}\left(\frac{\partial u_i}{\partial x_j}+\frac{\partial u_j}{\partial x_i}-\frac{2}{3}\delta_{ij}\frac{\partial u_k}{\partial x_k}\right) \quad (4)$$

where $\mu(T)$ is the nondimensional viscosity and $Re=u^*_\infty\rho^*_\infty\delta^*_1/\mu^*_\infty$ the Reynolds number. The viscous dissipation in the energy equation is calculated from

$$(\tau\boldsymbol{u})_i=\tau_{i1}u_1+\tau_{i2}u_2+\tau_{i3}u_3 \quad (5)$$

and the heat flux caused by conduction is given by

$$q_i=-\frac{\mu(T)}{(\gamma-1)RePrM^2_\infty}\frac{\partial T}{\partial x_i} \quad (6)$$

where Pr is the Prandtl number (for air $Pr=0.72$), $\gamma=c_p/c_v=1.4$ the ratio of specific heats, and M_∞ the free-stream Mach number. The nondimensional viscosity $\mu(T)$ is calculated from Sutherland's law:

$$\mu(T)=T^{\frac{3}{2}}[(1+s)/(T+s)] \quad (7)$$

where s is a parameter depending on the gas and the temperature range, set here to 110.3 K$/T^*_\infty$ for air. Closure of the Navier–Stokes equations still requires the calculation of the pressure. For a caloric perfect gas, the pressure is related to the conservative variables through

$$p=(\gamma-1)E-[(\gamma-1)/2]\rho\left(u_1^2+u_2^2+u_3^2\right) \quad (8)$$

Finally, the temperature can be calculated with the thermal equation of state for perfect gases,

$$T=\gamma M^2_\infty p\big/\rho \quad (9)$$

III. ADM with a Finite Volume Discretization

In most LES methods, filtering is performed implicitly by the projection of the equations onto the computational grid, formally including in the solution all wave numbers ω up to the Nyquist wave number ω_n (when considered after Fourier-transform into the wave-number space). Because for finite difference or finite volume schemes the wave number up to which scales can be considered to be well resolved is often significantly smaller than ω_n, it is desirable to suppress the nonresolved range of the solution by application of an explicit filter operation.[26] In the following we will distinguish between resolved wave numbers $|\omega|\le\omega_c$, where ω_c is the primary-filter cutoff wave number, represented wave numbers $|\omega|\le\omega_n$, which can be represented on the given mesh, and nonrepresented wave numbers $|\omega|>\omega_n$.

The governing equations of LES are obtained by applying a filter operation to the Navier–Stokes equations. The filtered quantity $\bar{f}$ is obtained by a convolution product with the filter kernel G_1 as

$$\bar{f}(x)=G_1*f=\int G_1(x-x')f(x')\,\mathrm{d}x' \quad (10)$$

where the bounds of the integral are defined by the compact support of the filter kernel. The integration in this definition is discretized by an explicit quadrature rule defined as

$$\bar{f}_i:=\sum_{j=-v_l}^{v_r}\alpha_j f_{i+j} \quad (11)$$

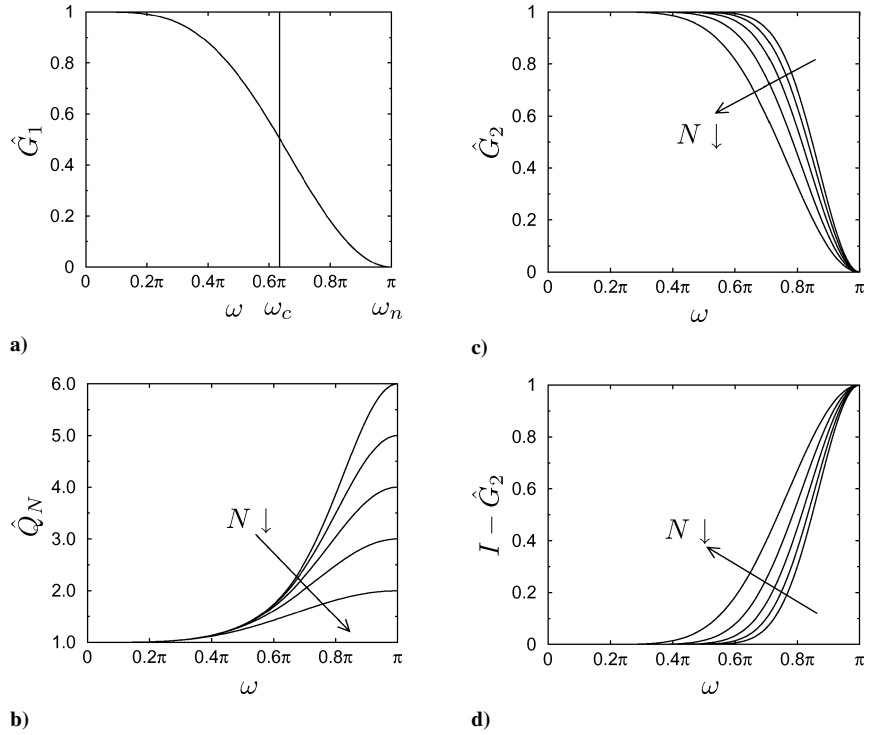

Fig. 1 Transfer functions on an equidistant mesh: a) primary filter $\hat{G}_1$, b) approximate inverse $\hat{Q}_N$ (note that $\hat{Q}_N(\pi) = N + 1$), c) secondary filter $\hat{G}_2 = \hat{Q}_N \cdot \hat{G}_1$, and d) $I - \hat{G}_2$ for decreasing deconvolution order from $N = 5$ to 1.

for the grid function f_i, where $f_i = f(x_i)$. Discrete filters on a five-point stencil with $\nu_l + \nu_r = 4$ for interior cells are considered. A complete derivation of the coefficients α_j can be found in Stolz et al.[21] and Stolz.[27] The definition of the cutoff wave number ω_c is somewhat arbitrary for filters with smooth Fourier transform $\hat{G}(\omega)$. Here the criterion $|\hat{G}_1(\omega_c)| = \frac{1}{2}$, leading to $\omega_c \approx 2/3\pi$ is used[20] (Fig. 1a).

The represented but nonresolved scales $\omega_c < |\omega| \leq \omega_n$ are used to model the effect of the nonrepresented scales $|\omega| > \omega_n$ on the resolved scales $|\omega| \leq \omega_c$. Represented scales can be recovered partially by an approximate inversion of the filter [eq. (10)] resulting in an approximation $f^\star$ of the unfiltered variable f. The approximate deconvolution $f^\star$ is obtained by applying an approximate deconvolution operator Q_N to $\bar{f}$:

$$f^\star = Q_N * \bar{f} \tag{12}$$

Assuming that the filter G_1 has an inverse, the inverse operator can be expanded as an infinite series of filter operators. Filters with compact transfer functions are noninvertible, but a regularized inverse operator Q_N can be obtained by truncating the series at some N, obtaining a regularized approximation[20] of G_1^{-1}:

$$Q_N = \sum_{\nu=0}^{N} (I - G_1)^\nu \approx G_1^{-1} \tag{13}$$

where I is the identity operator. A plot of the transfer function $\hat{Q}_N$ is shown on Fig. 1b for deconvolution order N varying from 1 to 5.

Stolz et al.[21] found that the deconvolution order $N = 5$ was giving very good results for a wide range of test cases. However, in the frame of the present work it was found that adapting the deconvolution order locally to the flow accounted for a better modeling of the energy dissipation mechanism. Substituting Eq. (13) into Eq. (12), $f^\star$ can be computed by repeated filtering of $\bar{f}$ from

$$\begin{aligned} f^\star = Q_N * \bar{f} &= \bar{f} + (\bar{f} - \bar{\bar{f}}) + (\bar{f} - 2\bar{\bar{f}} + \bar{\bar{\bar{f}}}) + \dots \\ &= 3\bar{f} - 3\bar{\bar{f}} + \bar{\bar{\bar{f}}} + \dots \end{aligned} \tag{14}$$

The extension of ADM to a finite volume scheme is obtained by applying the explicit filter operation [Eq. (10)] and deconvolution [Eq. (13)] to the cell-averaged values. Note that a finite volume scheme itself involves the application of a top-hat filter when cell-average values are computed and a deconvolution operation when cell-face values are reconstructed from the cell averages (e.g., see Adams[28]). Here, however, the numerical discretization and subgrid-scale modeling are treated as separate processes. We rewrite Eq. (1) as

$$\frac{\partial \boldsymbol{U}}{\partial t} + \nabla \cdot \mathbb{F}(\boldsymbol{U}) = 0 \tag{15}$$

where $\mathbb{F}(\boldsymbol{U}) = (\boldsymbol{f}_{\text{inv}} - \boldsymbol{f}_v, \boldsymbol{g}_{\text{inv}} - \boldsymbol{g}_v, \boldsymbol{h}_{\text{inv}} - \boldsymbol{h}_v)$ is the flux tensor. After integrating the preceding equation over some volume V and applying the divergence theorem, it can be rewritten as

$$\int_V \frac{\partial \boldsymbol{U}}{\partial t} \, \mathrm{d}\mathcal{V} + \int_S \mathbb{F}(\boldsymbol{U}) \boldsymbol{n} \, \mathrm{d}\mathcal{S} = 0 \tag{16}$$

with $\boldsymbol{n} = (n_1, n_2, n_3)$ being the outward normal vector of the cell surface S.

The discretization for the ith cell of volume V_i and cell-average $\boldsymbol{U}_i = 1/V_i \int_{V_i} \boldsymbol{U} \, \mathrm{d}\mathcal{V}$ is given by (the indices are written for a one-dimensional case for notational simplicity without loss of generality)

$$\frac{\partial \boldsymbol{U}_i}{\partial t} + \frac{1}{V_i} \sum_{j=1}^{n_{\text{faces}}} \boldsymbol{F}_{ij}(\boldsymbol{U}) \cdot S_j = 0 \tag{17}$$

where $\boldsymbol{F}_{ij}(\boldsymbol{U})$ is the discrete flux through the jth cell face of the ith cell and n_{faces} are the number of faces of the cell.

In the framework of the finite volume formulation, the cell-average values located in the cell centers constitute the discrete grid function on which the discrete filter [Eq. (11)] is applied. The filtered cell-average value is defined as

$$\bar{\boldsymbol{U}}_i = G_1|_i * \boldsymbol{U}_i := \sum_{k=-\nu_l}^{\nu_r} \alpha_k \boldsymbol{U}_{i+k} = \sum_{k=-\nu_l}^{\nu_r} \alpha_k \left[\frac{1}{V_{i+k}} \int_{V_{i+k}} \boldsymbol{U} \, \mathrm{d}\mathcal{V} \right] \tag{18}$$

where the volume of the cell, which is a function of space for irregular grids, has to be included in the filter operation. Applying the discrete filter [Eq. (18)] to the discrete transport equation (17) yields

$$G_1|_i * \frac{\partial \boldsymbol{U}_i}{\partial t} + G_1|_i * \left[\frac{1}{V_i} \sum_{j=1}^{n_{\text{faces}}} \boldsymbol{F}_{ij}(\boldsymbol{U}) \cdot S_j \right] = 0 \qquad (19)$$

Using the approximately deconvolved solution $\boldsymbol{U}^\star = Q_N * \bar{\boldsymbol{U}}$, the filtered flux can be approximated directly by replacing the unfiltered quantity $\boldsymbol{U}$ by $\boldsymbol{U}^\star$, so that the left-hand side of Eq. (19) becomes

$$\frac{\partial \bar{\boldsymbol{U}}_i}{\partial t} + G_1|_i * \left[\frac{1}{V_i} \sum_{j=1}^{n_{\text{faces}}} \boldsymbol{F}_{ij}(\boldsymbol{U}^\star) \cdot S_j \right] \qquad (20)$$

thus avoiding at this point the need of computing extra subgrid-scale terms.

The energy transfer to nonrepresented scales $|\omega| > \omega_n$ is modeled only partially by using $\boldsymbol{U}^\star$ in Eq. (20). Stolz et al.[14,21] proposed a relaxation regularization derived from the requirement that the solution remains well resolved within the range $|\omega| \le \omega_c$. For this purpose, the integral energy of the nonresolved represented scales should not increase, although energy redistribution among these scales is permitted. To model the energy transfer from scales $|\omega| \le \omega_n$ to scales $|\omega| > \omega_n$, energy is drained from the range $\omega_c < |\omega| \le \omega_n$ by subtracting a relaxation term $\chi(I - G_2) * \bar{\boldsymbol{U}}$ [multiplication between the components of the vector $\chi = (\chi_1, \chi_2, \chi_2, \chi_2, \chi_3) = (\chi_\rho, \chi_{\rho|u|}, \chi_{\rho|u|}, \chi_{\rho|u|}, \chi_E)$ and those of the vector $(I - G_2) * \bar{\boldsymbol{U}}$] from the right-hand side of the filtered differential conservation law [Eq. (20)]. This expression has the form of a relaxation term with relaxation coefficients $\chi_k, k = 1, \ldots, 3$ corresponding to an inverse relaxation-time scale. G_2 is a secondary filter with larger cutoff wave number than the primary filter G_1 and is chosen here as $G_2 = Q_N * G_1$. The transfer function of the secondary filter G_2 for an equidistant mesh, for example, in the x_2 direction, is shown in Fig. 1c for a deconvolution order N varying from 1 to 5. Because $(I - \hat{G}_2)$ is positive semidefinite by construction, the relaxation term is purely dissipative as long as χ is positive. Note also that $(I - \hat{G}_2)$ essentially vanishes for $\omega < \omega_c$, that is, the relaxation term leaves the resolved scales untouched. Subtracting the relaxation term from the right-hand side gives the complete ADM formulation for finite volumes

$$\frac{\partial \bar{\boldsymbol{U}}_i}{\partial t} + \overline{\frac{1}{V_i} \sum_{j=1}^{n_{\text{faces}}} \boldsymbol{F}_{ij}(\boldsymbol{U}^\star) \cdot S_j} = -\chi(I - G_2) * \bar{\boldsymbol{U}}_i \qquad (21)$$

with the flux vector (summation over repeated indices, $l, m = 1, 2, 3$)

$$\boldsymbol{F}_{ij}(\boldsymbol{U}^\star) = \begin{pmatrix} (\rho u_m)^\star n_m \\ (\rho u_1)^\star \dfrac{(\rho u_m)^\star}{\rho^\star} n_m + \check{p}^\star n_1 - \check{\tau}^\star_{1m} n_m \\ (\rho u_2)^\star \dfrac{(\rho u_m)^\star}{\rho^\star} n_m + \check{p}^\star n_2 - \check{\tau}^\star_{2m} n_m \\ (\rho u_3)^\star \dfrac{(\rho u_m)^\star}{\rho^\star} n_m + \check{p}^\star n_3 - \check{\tau}^\star_{3m} n_m \\ (E^\star + \check{p}^\star) \dfrac{(\rho u_m)^\star}{\rho^\star} n_m - \check{\tau}^\star_{ml} \dfrac{(\rho u_l)^\star}{\rho^\star} n_m - \check{q}^\star_m n_m \end{pmatrix}_{ij} \qquad (22)$$

The notation $\check{}^\star$ indicates that the respective quantities are computed from the deconvolved solution, for example, $\check{p}^\star = (\gamma - 1)[E^\star - (\rho u_i)^\star(\rho u_i)^\star/(2\rho^\star)]$.

To close the model without requiring an a priori parameter choice, Stolz et al.[14,21] estimate χ dynamically from the current solution $\bar{\boldsymbol{U}}$ as a function of space and time. The underlying argument for determining χ is that in order to obtain a well-resolved representation of the filtered solution no energy should accumulate during time advancement in the wave-number range $\omega_c < |\omega| \le \omega_n$. The kinetic energy content of the considered wave-number range can be estimated by the second-order structure function[29,30] H_k applied to $\phi_k = (I - G_2) * \bar{W}_k$, where $W_1 = \rho$, $W_2 = \rho|\boldsymbol{u}|$, and $W_3 = E$. The discrete form of the local second-order structure function in three dimensions, which requires the value of ϕ_k at the considered grid point in the computational space $\xi = (\xi_1, \xi_2, \xi_3)$ and its six next neighbors in the three computational-space coordinate directions, is given by

$$H_k(\xi, t) = \|\phi_k(\xi + \boldsymbol{r}, t) - \phi_k(\xi, t)\|^2_{\|r\| = h} \qquad (23)$$

Note again that the mapping of the physical space onto the computational space does not need to be known explicitly.

For an estimate of the relaxation parameter χ_k, Eq. (21) is advanced by one Euler-forward time step with size Δt, once using $\chi_k = \chi_{k0}$ and once using $\chi_k = 0$. χ_{k0} is some positive nonvanishing estimate of the parameter χ_k, for example, the value from the preceding time-integration step or some positive constant of the order of $1/\Delta t$ at time $t = 0$. The difference of the structure function $H_k(\xi, t + \Delta t)|_{\chi_k = 0} - H_k(\xi, t)$ is an estimate for the integral energy generated within the time increment Δt in the range of scales with wave numbers $\omega_c < |\omega| \le \omega_n$. The difference $H_k(\xi, t + \Delta t)|_{\chi_k = 0} - H_k(\xi, t + \Delta t)|_{\chi_k = \chi_{k0}}$ estimates how much energy would be dissipated by the relaxation term using $\chi_k = \chi_{k0}$. Accordingly, χ_k can be determined from

$$\chi_k = \chi_{k0} \frac{H_k(\xi, t + \Delta t)|_{\chi_k = 0} - H_k(\xi, t)}{H_k(\xi, t + \Delta t)|_{\chi_k = 0} - H_k(\xi, t + \Delta t)|_{\chi_k = \chi_{k0}}} \qquad (24)$$

By construction, the dynamic parameter χ_k is now a function of space and time. To avoid the generation of nonresolved scales as a result of the nonlinear product of χ and $(I - G_2) * \bar{\boldsymbol{U}}$, χ_k is smoothed with a second-order Padé filter,[31] whose cutoff wave number ω'_c is set to $\pi/8$. Given a time-step size Δt, an upper and a lower bound $1/100\Delta t \le \chi_k \le 1/\Delta t$ is imposed for numerical stability at the given time step. If higher values of χ_k are admitted, Δt has to be decreased accordingly.

The use of the relaxation term can also be interpreted as applying a secondary filter to $\bar{\boldsymbol{U}}$ every $1/\chi_k$ time steps, which poses the approach in a relation to the truncated Navier–Stokes approach with energy removal of Domaradzki and Radhakrishnan[32] or the implicit LES approach with periodic filtering of the solution of Visbal et al.[33]

IV. Application to the Compression Ramp Flow

Following the flow configuration of Adams,[19] the turbulent boundary layer along a compression ramp with a deflection angle of 18 deg at a freestream Mach number of $M = 3$ and Reynolds number of $Re_\theta = 1685$ with respect to freestream quantities and mean momentum thickness at inflow is computed by LES with ADM. Figure 2 gives a schematic representation of the flow.

The variables are nondimensionalized as mentioned earlier. The fluid is assumed to be a perfect gas, and the viscosity is calculated according to Sutherland's law with the freestream temperature as reference. Table 1 gives an overview of the parameters of the simulation. At inflow, turbulent boundary-layer data obtained from filtering a separate DNS from Adams[19] are imposed. To avoid a reflection of the shock, nonreflecting boundary conditions[34] are used at the outflow and on the upper boundary of the computational domain. No-slip isothermal conditions are applied at the wall, and the flow is periodic in the spanwise direction.

Tests realized with a second- and fourth-order discretization showed that the latter discretization reduced the oscillations amplitudes in the vicinity of the discontinuity and was therefore preferred here. To take advantage of its intrinsic dealiasing property, the convective terms are formulated in skew-symmetric form.[35] For a generic flux $f = uv$, the fourth-order central discretization reads then (see Ref. 36),

$$f_{i+\frac{1}{2}} = \tfrac{1}{3}(u_i + u_{i+1})(v_i + v_{i+1}) - (1/24)(u_{i-1}v_{i-1} + u_{i-1}v_{i+1} + u_i v_i + u_i v_{i+2} + u_{i+1}v_{i+1} + u_{i+1}v_{i-1} + u_{i+2}v_i + u_{i+2}v_{i+2}) \qquad (25)$$

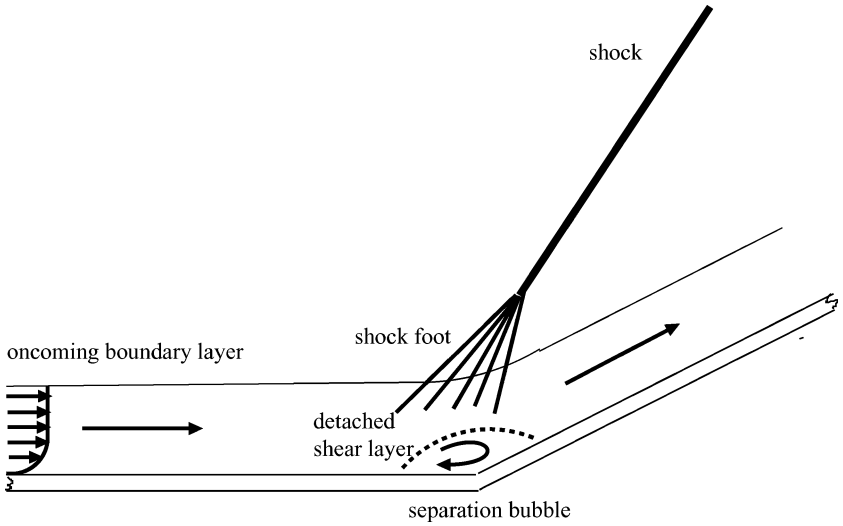

Fig. 2 Sketch of the compression ramp flow configuration.

Table 1 Parameters of the numerical simulation

Parameter[a]	Value	Comment
M_∞	3	Freestream Mach number
Re_{δ_1}	8977	Reynolds number based on the displacement thickness at the inflow (station 0), $Re_{\delta_1} = u_\infty \rho_\infty \delta_1 / \mu_\infty$
Re_θ	1685	Reynolds number based on the momentum thickness at the inflow and ν_∞
Re_{δ_2}	732	Reynolds number based on the momentum thickness at the inflow and ν_w
δ_0	2.38	Boundary-layer thickness at inflow
θ	0.19	Momentum thickness at inflow
T^*_∞	115 K	Freestream temperature
T^*_w	2.522 T^*_∞	Wall temperature
s^*	110.4 K	Sutherland's law constant
β	18 deg	Compression ramp angle
L_1	63.80	Streamwise extent of the computational domain
L_2	2.90	Spanwise extent of the computational domain
L_3	10.87	Wall normal extent of the computational domain at the inflow
L_3	21.40	Wall normal extent of the computational domain at the outflow
N_1	332	Number of cells in streamwise dimension (1/3 of DNS by Adams[19])
N_2	30	Number of cells in spanwise dimension (3/8 of DNS by Adams[19])
N_3	90	Number of cells in wall normal dimension (1/2 of DNS by Adams[19])
$\Delta_1^+\|_w$	18	Streamwise cell size in wall units at inflow
$\Delta_2^+\|_w$	8.8	Spanwise cell size in wall units at inflow
$\Delta_3^+\|_w$	1.4	Wall normal cell size in wall units at inflow
$\Delta_1^+\|_w$	37.8	Streamwise cell size in wall units at station 10
$\Delta_2^+\|_w$	20.4	Spanwise cell size in wall units at station 10
$\Delta_3^+\|_w$	4.3	Wall normal cell size in wall units at station 10

[a]Subscript w = wall values.

for the flux at cell face $i + \frac{1}{2}$ (similar for the other faces). The viscous fluxes are computed using the gradient theorem on a shifted volume.[37] The time integration is performed with an explicit low-storage four-stage Runge–Kutta scheme where an adaptive time step based on a linear stability analysis is used.[25]

V. Results

To represent the turbulent flow and the shock properly, the computational mesh required $\frac{1}{3}$ of the number of points of the DNS of Adams[19] in the streamwise direction, $\frac{3}{8}$ in the spanwise direction and $\frac{1}{2}$ in the wall-normal direction, leading to $N_1 = 332$, $N_2 = 30$, $N_3 = 90$ cells. Grid-resolution studies have shown that the present spatial resolution and temporal integration period give fully converged and stable results.[24]

The simulation was started with interpolated DNS data from Adams, and sampling was performed after an initial transient of 100 time units when a statistically steady state was reached. The infow data during the simulation were obtained by spatial and temporal interpolation of the DNS solution of Adams. Angles $\langle\,\rangle$ indicate spanwise- and time averaging, and Favre filtered variables are denoted by $\tilde{f} = \overline{\rho f}/\bar{\rho}$. To obtain a consistent definition across the integration domain, in particular near the corner of the ramp, the velocity vector is projected to a Cartesian system aligned with the wall. The contravariant velocities $\tilde{u}_i^c$ are defined as

$$\tilde{u}_1^c = \frac{\tilde{u}_1(\partial\xi_1/\partial x_1) + \tilde{u}_3(\partial\xi_1/\partial x_3)}{\sqrt{(\partial\xi_1/\partial x_1)^2 + (\partial\xi_1/\partial x_3)^2}}$$

$$\tilde{u}_2^c = \tilde{u}_2$$

$$\tilde{u}_3^c = \frac{\tilde{u}_1(\partial\xi_3/\partial x_1) + \tilde{u}_3(\partial\xi_3/\partial x_3)}{\sqrt{(\partial\xi_3/\partial x_1)^2 + (\partial\xi_3/\partial x_3)^2}} \tag{26}$$

where ξ_i = constant defines the grid lines of the computational mesh.

The remainder of this section is organized in two parts. First, the effect of the deconvolution order on the flow solution is examined. Second, based on the observations of the effect of the different deconvolution orders, the results of the supersonic compression ramp flow with the deconvolution order being locally adapted to the flow are presented and compared to DNS results.

A. Effect of the Deconvolution Order

The difficulty for the subgrid-scale modeling consists in representing accurately the turbulence in the boundary layer, the detached shear layer of the separation bubble, and the sharp gradients of the shock. We recall that a central scheme is used and that this kind of discretization generates oscillations in the vicinity of a discontinuity leading to nonlinear instability. A solution to prevent these oscillations would be to use an upwind scheme locally in the shock vicinity or to switch on artificial dissipation terms. This approach was consciously not followed in this evaluation phase of ADM with the finite volume method because the effect of the subgrid-scale model would have been inseparable from the dissipation of the upwind scheme or from the artificial dissipation terms. The aim here is to obtain a stable and accurate representation of the discontinuity by acting on the subgrid-scale model instead of the discretization scheme, and we therefore focus on suitably adapting the deconvolution order of the inverse filter [Eq. (13)] of ADM.

In Eq. (21), the deconvolution order influences the deconvolved quantity

$$\boldsymbol{U}^{\star} = Q_N * \bar{\boldsymbol{U}} = \sum_{\nu=0}^{N} (I - G_1)^{\nu} * \bar{\boldsymbol{U}}$$

and the relaxation term $-\chi(I - G_2) * \bar{\boldsymbol{U}}$. Reducing the deconvolution order has thus a double effect. First, the deconvolved quantity $\boldsymbol{U}^{\star}$ will be a poorer approximation of the exact unfiltered quantity $\boldsymbol{U}$, provided that the scales near the filter cutoff are well represented by the numerical discretization. For low-order schemes (including the fourth-order scheme used here), the error for wave numbers near the cutoff is significantly larger than with a spectral representation.[31] In this case, high-order deconvolution often only amplifies numerical noise and is not desired. The small-scale amplification effect with increasing deconvolution order N of the approximate inverse filter Q_N can be seen in Fig. 1b. Second, the wave-number range from which energy is removed by the relaxation term will grow towards larger scales when reducing N, damping larger-scale oscillations as they develop in the vicinity of a discontinuity. The increase of the range of scales being damped by the secondary filter G_2 with decreasing deconvolution order N can be seen in Fig. 1c. Although the mathematical formulation is quite different, the effect of the relaxation term on the flow is comparable to a numerical dissipation term, for example, the Jameson dissipation[38] and the reduction of the deconvolution order smoothes the solution in a similar way as artificial numerical dissipation. The difference between the two approaches resides in the fact that ADM adds a relaxation term (operating only on nonresolved wave numbers), whereas classical numerical dissipation adds high-order derivative terms to the conservation law.

By applying the same deconvolution order ($N = 5$) that had given good results for the supersonic channel flow,[23] the oscillations near the shock permitted by the central schemes were not sufficiently damped and slowly grew and propagated away from the discontinuity until the calculation became unstable. Stable computations were obtained by reducing the deconvolution order, but the solution deteriorated then in the boundary layer where the cumulated effect of the physical viscosity and the low-order relaxation regularization showed an overdissipative behavior. The contradictory requirement of having a small dissipation in the boundary layer and sufficient dissipation in the vicinity of the discontinuity was solved by varying the order of deconvolution as a function of the distance to the wall. The positive effect of the variable deconvolution order on the skin-friction coefficient, which measures the velocity gradient at the wall, can be seen in Fig. 3a. Low-order deconvolution ($N = 1$) near the wall clearly underpredicts the wall velocity gradient which is typical of an overdissipative behavior. The insufficient damping of the large scales oscillations is set in evidence in Fig. 3b, where the rms fluctuations of the density and the Favre-averaged fluctuations of the Reynolds stress are overpredicted in the vicinity of the shock when using a third-order deconvolution. (The same trend is observed for the other fluctuating quantities, but the differences in the mean quantities are only minimal.) The results obtained with decreasing deconvolution order as a function of the wall distance show a better agreement with the reference data in the near-wall region (Fig. 3a), in the boundary layer and in the shock vicinity (Fig. 3b). Expressed in wall units ($^+$), the deconvolution order is set to $N = 5$ for $x_3^+ \lesssim 20$, $N = 4$ for $20 \lesssim x_3^+ \lesssim 40$, $N = 3$ for $40 \lesssim x_3^+ \lesssim 200$, $N = 2$ for $200 \lesssim x_3^+ \lesssim 240$, $N = 1$ for $x_3^+ \gtrsim 240$, and has a similar effect in principle as a wall-damping function (e.g., van Driest correction) although the mathematical formulation of the two approaches is completely different. With this repartition, the viscous-wall region ($x_3^+ \lesssim 50$) is situated in the high deconvolution order region, whereas the shock is entirely located in the $N = 1$ area. Between the two extrema, the deconvolution order varies gradually (Fig. 4).

Additional results on the effect of the deconvolution order, its influence on the relaxation coefficient χ, and relaxation term $-\chi(I - G_2) * \bar{\boldsymbol{U}}$ are presented in the Appendix for the test problem of shock-wave propagation in a shock tube.

B. Local Adaptation of the Deconvolution Order

Based on the results of the preceding subsection and of the Appendix, the benefit of the variable deconvolution order has become obvious, and all of the results discussed further were obtained with decreasing deconvolution order as a function of the wall distance as described there.

The density gradient magnitude averaged over the spanwise direction, displayed in Fig. 5, gives an overview of the flow. The DNS of Adams[19] is shown on the left and the LES on the right. The

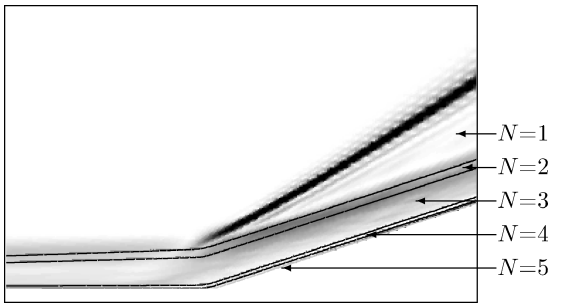

Fig. 4 Decreasing deconvolution order N as a function of the wall distance with the density gradient magnitude shown in background: $N = 5$ for $x_3^+ \lesssim 20$, $N = 4$ for $20 \lesssim x_3^+ \lesssim 40$, $N = 3$ for $40 \lesssim x_3^+ \lesssim 200$, $N = 2$ for $200 \lesssim x_3^+ \lesssim 240$, and $N = 1$ for $240 \lesssim x_3^+$.

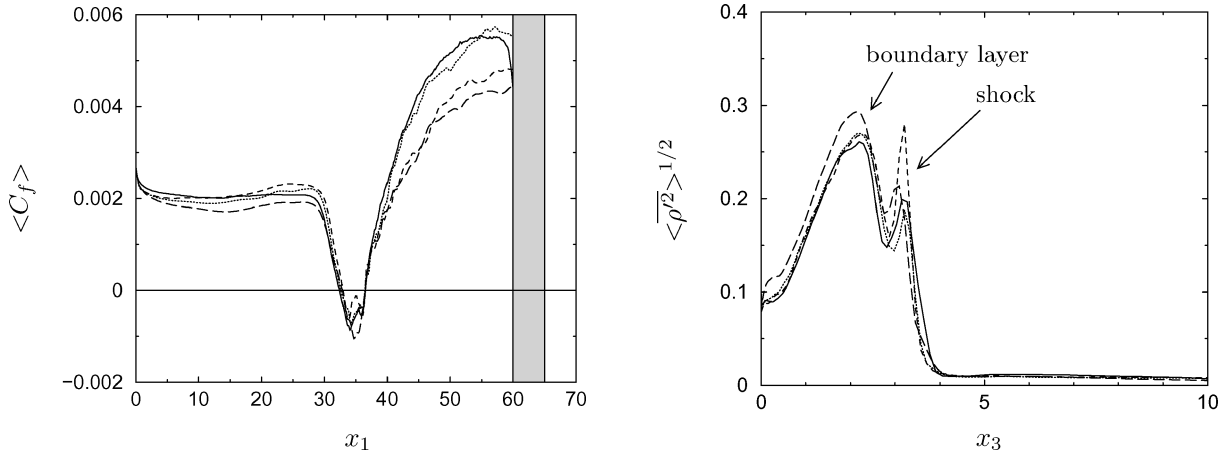

Fig. 3 Effect of the deconvolution order: a) friction coefficient $\langle C_f \rangle$: ——, DNS; b) density rms fluctuations $\langle \bar{\rho}'^2 \rangle^{1/2}$ at station 9 of Fig 6: ——, filtered DNS; . . . . , decreasing deconvolution order from $N = 5$ near the wall to $N = 1$ above the boundary layer; - - - -, constant deconvolution order $N = 3$; and - - - -, constant deconvolution order $N = 1$. The shaded area of graph (3a) indicates the sponge region used as outflow boundary treatment in the DNS.

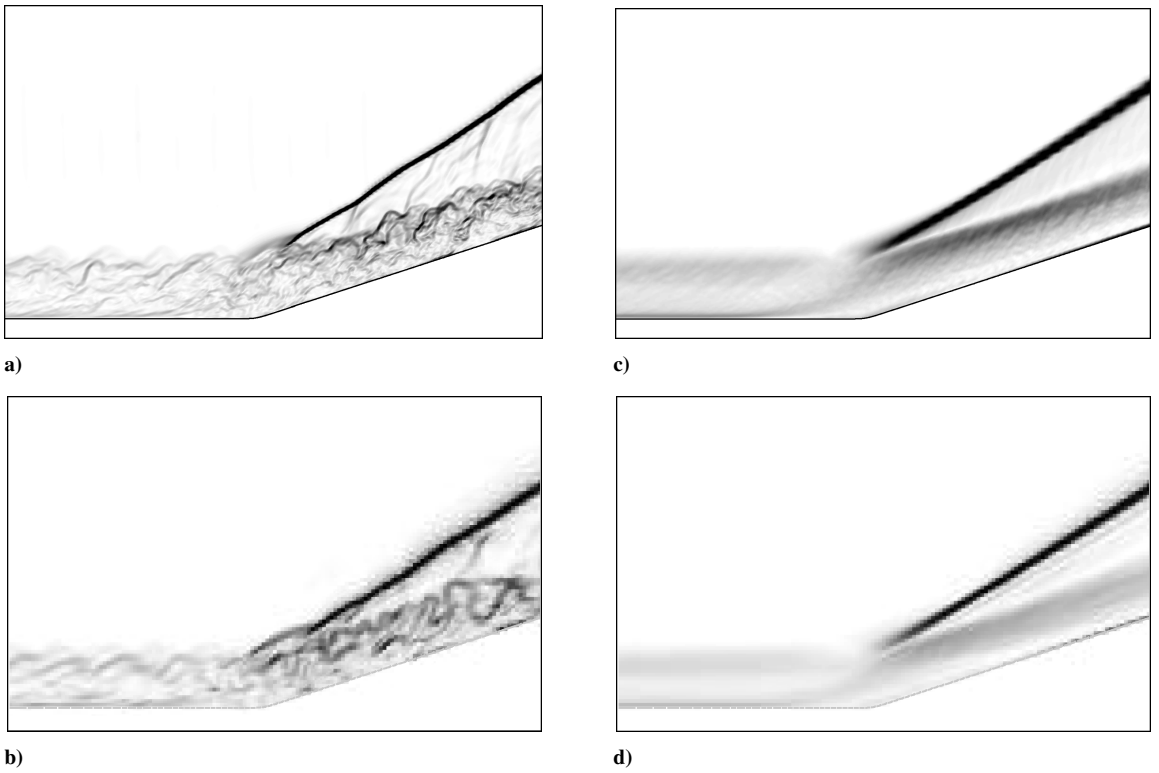

Fig. 5 Flowfield schlieren imitatin by $\|\nabla_\rho\|$ contours: a) spanwise-averaged DNS (Adams[19]), b) spanwise-averaged LES, c) spanwise- and time-averaged DNS, and d) spanwise- and time-averaged LES. The streamwise extent of the snapshot is from $x_1 \approx 25$ to 50.

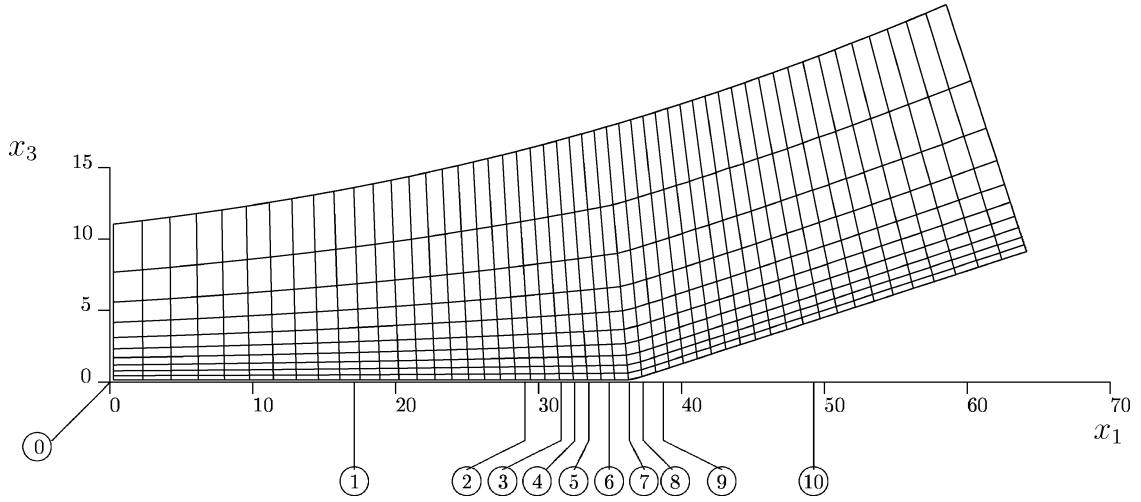

Fig. 6 Computational mesh (each ninth line is shown); numbers in circles indicate stations where profiles are shown in the following graphs.

instantaneous density gradient (Fig. 5a and 5b) corresponds to different flow realizations and can only be compared qualitatively. It can be seen that, because of the coarser mesh, the shock of the LES is slightly more smeared out, but overall the LES exhibits the same flow patterns as the DNS.

For the mean and turbulent profiles, we compare LES-ADM results with the filtered DNS results of Adams at 10 different downstream stations along the computational mesh lines (Fig. 6). The time averaging covers 150 time units with a sampling period of 0.1. All mean profiles are very well predicted. Figures 7 and 8 show the Favre-averaged filtered contravariant velocity, temperature, pressure, and density profiles. Only small wiggles are observed near the shock, and the shock position and the boundary layer are very well predicted by the LES. The same trend can be observed for the contravariant momentum displayed in Fig. 9. The van Driest transformed mean streamwise velocity $\langle\tilde{u}_1^c\rangle_{\mathrm{VD}}^+$ for a compressible boundary layer is defined as

$$\left\langle\tilde{u}_1^c\right\rangle_{\mathrm{VD}}^+ = \int_0^{\langle\tilde{u}_1^c\rangle^+} \sqrt{\frac{\bar{\rho}}{\bar{\rho}_w}}\, d\left\langle\tilde{u}_1^c\right\rangle^+ \tag{27}$$

This transformation accounts for the density variation across the boundary layer and allows for comparison with the logarithmic law of the velocity profile $2.5\,\ell_n x_3^+ 5.5$. Figure 10 shows the mean and van Driest transformed velocity profile scaled in wall units before (station 1) and after (station 10) the corner. As no shock is present before the compression corner, the flow is identical with a supersonic boundary layer, and the agreement of the LES with the filtered DNS and the logarithmic law is very good. However, behind the compression corner the shock crosses the upper part of the computational domain, and deviations from the logarithmic law can be observed in

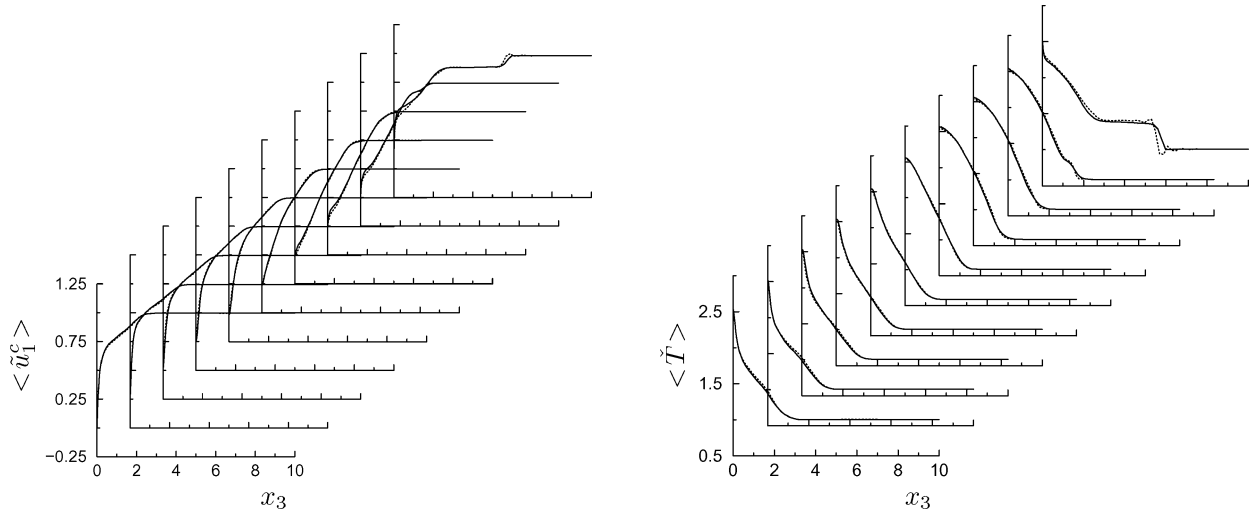

a) b)

Fig. 7 Favre-averaged variables: a) contravariant velocity $\langle \tilde{u}_1^c \rangle$ and b) temperature $\langle \check{T} \rangle$, at the steamwise stations 1–10 according to Fig. 6: ——, filtered DNS and . . . . , LES with ADM; superscript $\breve{\bullet}$ indicates that the quantity is computed from the filtered solution.

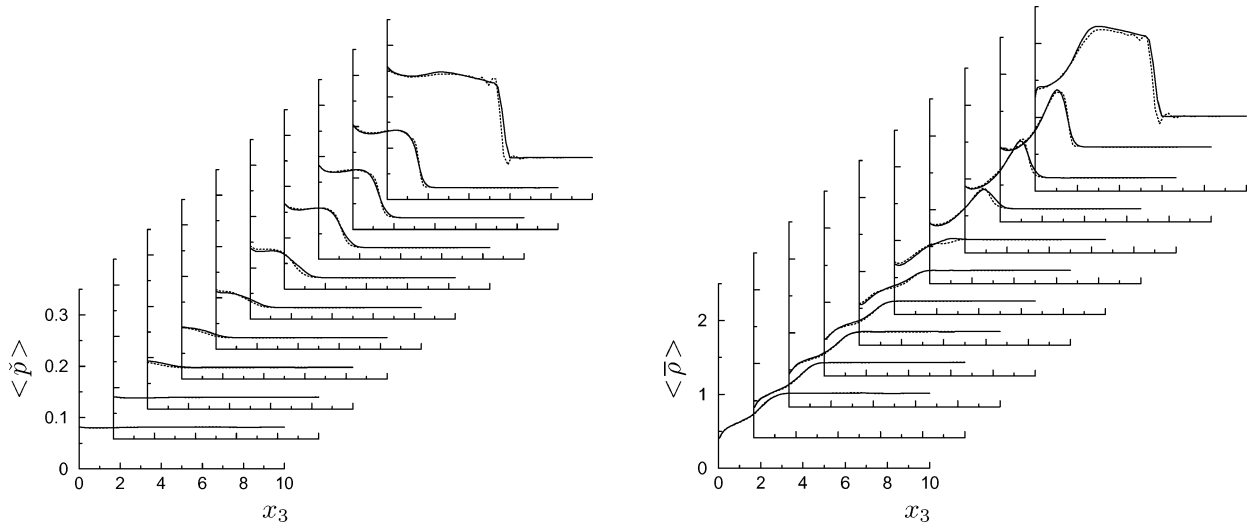

a) b)

Fig. 8 Favre-averaged variables: a) pressure $\langle \check{p} \rangle$ and b) density $\langle \bar{\rho} \rangle$, at the steamwise stations 1–10 according to Fig. 6: ——, filtered DNS and . . . . , LES with ADM; superscript $\breve{\bullet}$ indicates that the quantity is computed from the filtered solution, for example, $\check{p} = (\gamma - 1)\,[\bar{E} - \overline{\rho u_i}\,\overline{\rho u_i}/(2\bar{\rho})]$.

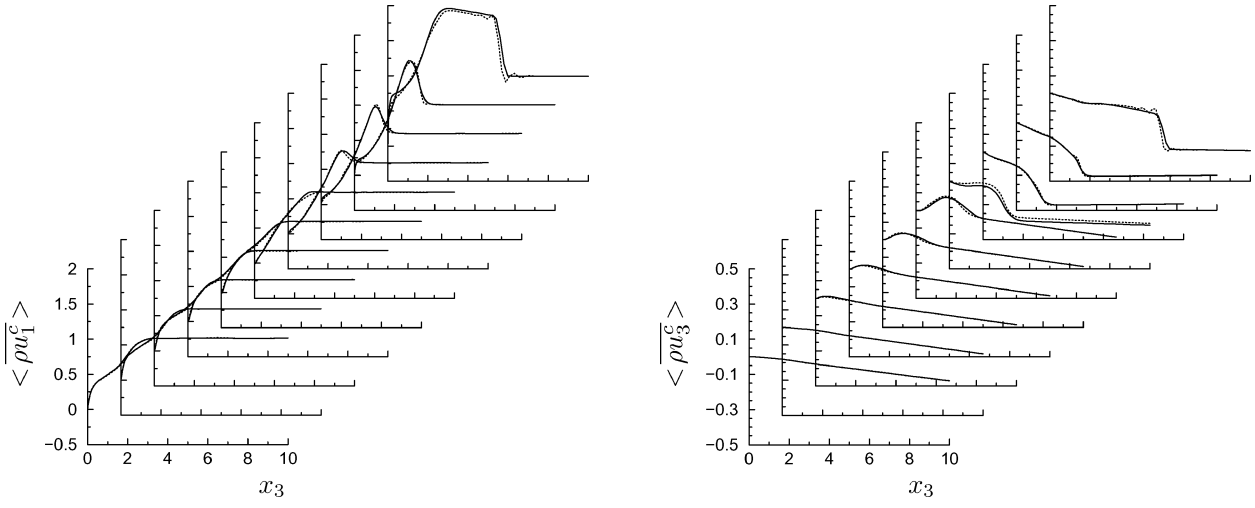

a) b)

Fig. 9 Contravariant momentum a) streamwise $\langle \overline{\rho u_1^c} \rangle$ and b) wall normal $\langle \overline{\rho u_3^c} \rangle$, at the steamwise stations 1–10 according to Fig. 6: ——, filtered DNS and . . . . , LES with ADM.

Fig. 10b. Some discrepancy between the filtered DNS and the LES can also be seen in the vicinity of the shock.

Wall quantities are among the most difficult quantities to predict correctly. Figure 11a shows the skin-friction coefficient $\langle C_f \rangle = 2\mu \langle \partial u / \partial x_3 \rangle|_{\text{wall}}$, which is in very good agreement with the filtered DNS and gives the correct location and length of the flow separation around the corner (region where $\langle C_f \rangle \leq 0$). The wall pressure (Fig. 11b) shows also excellent agreement with the filtered DNS.

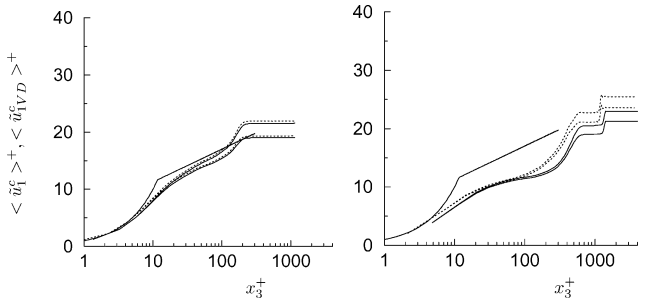

a) b)

Fig. 10 Contravariant velocity profile scaled in wall units at a) station 1 and b) station 10: for mean velocity $\langle \tilde{u}_1^c \rangle^+$, —— and filtered DNS; . . . . , ADM; and for van Driest transformed mean velocity $\langle \tilde{u}_{1VD}^c \rangle^+$, ——, filtered DNS; . . . . , ADM; and ——, linear and logarithmic law ($2.5\,\ell_n\, x_3^+ + 5.5$).

The turbulent fluctuations of the flow are analyzed by means of the Reynolds- and the Favre-averaged fluctuations, which are computed as $f' := f - \langle f \rangle$ and $f'' := f - \langle \bar{\rho} f \rangle / \langle \bar{\rho} \rangle$, respectively. The overall agreement between filtered DNS and LES is very good as can be seen for the density rms fluctuations $\langle \bar{\rho}'^2 \rangle^{1/2}$, the temperature Favre-averaged fluctuations $\langle \check{T}''^2 \rangle^{1/2}$ (Fig. 12), the streamwise contravariant momentum rms fluctuations $\langle \overline{\rho u}_1^{c''2} \rangle^{1/2}$, and the streamwise contravariant velocity Favre-averaged fluctuations $\langle \tilde{u}_1^{c''2} \rangle^{1/2}$ (Fig. 13). The fluctuations within the boundary layer (first peak) and around the shock (second peak) are very well represented except for a slight discrepancy visible in the boundary layer around the corner of the ramp (stations 6–9), which coincides also with the foot of the shock. The same trend is observed for the Reynolds-stress Favre-averaged fluctuations $\langle \bar{\rho} \tilde{u}_1^{c''} \tilde{u}_1^{c''} \rangle$, $\langle \bar{\rho} \tilde{u}_2^{c''} \tilde{u}_2^{c''} \rangle$, $\langle \bar{\rho} \tilde{u}_3^{c''} \tilde{u}_3^{c''} \rangle$, and $\langle \bar{\rho} \tilde{u}_1^{c''} \tilde{u}_3^{c''} \rangle$ shown in Figs. 14 and 15. The maximum deviation is less than 10% and occurs in the area of the corner of the ramp.

In comparison with the results of Stolz et al.[14] obtained with the same grid resolution but with a sixth-order compact finite difference scheme, the mean and turbulent statistics here are of the same quality despite the lower-order numerical method. This is of special interest for industrial applications where the finite volume method is widely used and high-order schemes are normally unaffordable. The price for the low-order numerical scheme is that local adaptation of the deconvolution order was necessary, whereas Stolz et al. used the deconvolution order $N = 5$ throughout the whole computational domain.

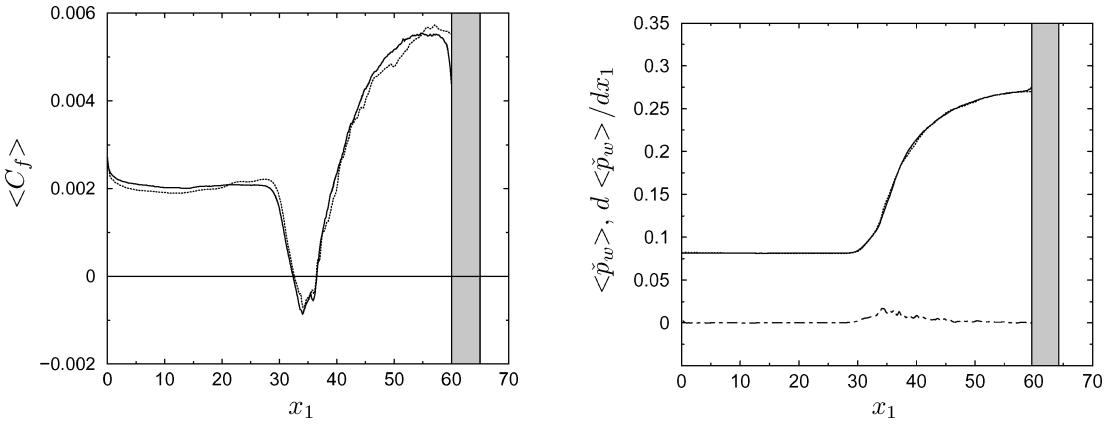

a) b)

Fig. 11 Wall quantities: a) skin-friction coefficient $\langle C_f \rangle$, where ——, DNS and . . . . , ADM; b) wall pressure $\langle \check{p}_w \rangle$, where ——, DNS; . . . . , ADM; and streamwise pressure gradient: $d\langle \check{p}_w \rangle / dx_1$, whereas —.—, ADM. The shaded area of panel a indicates the sponge region used as outflow boundary treatment in the DNS.

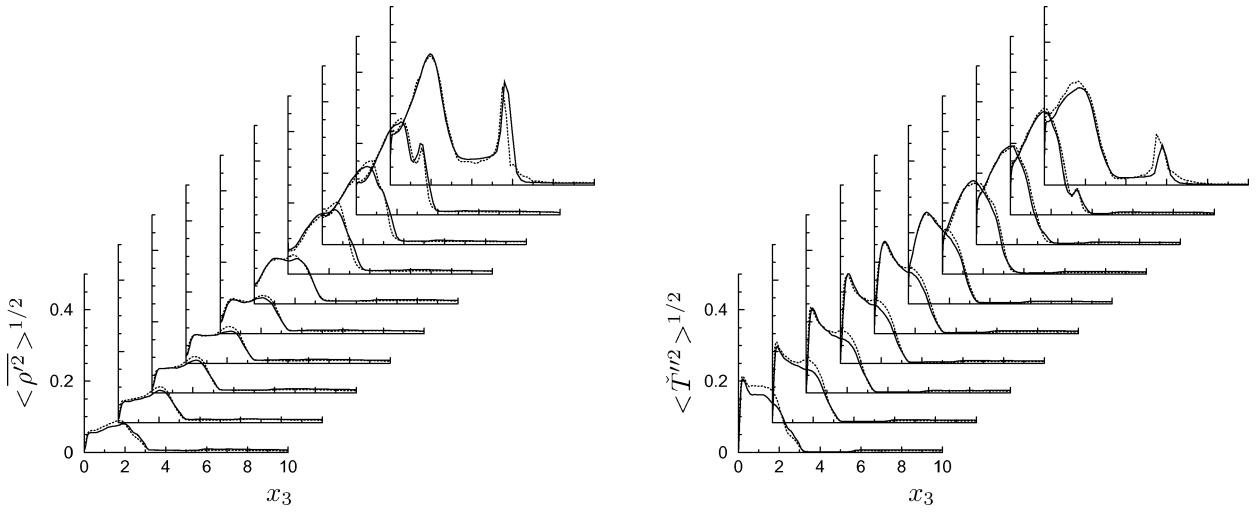

a) b)

Fig. 12 Turbulent fluctuations: a) density rms fluctuations $\langle \bar{\rho}'^2 \rangle^{1/2}$ and b) Favre-averaged temperature fluctuations $\langle \check{T}''^2 \rangle^{1/2}$, at the streamwise stations 1–10 according to Fig. 6: ——, filtered DNS and . . . ., LES with ADM.

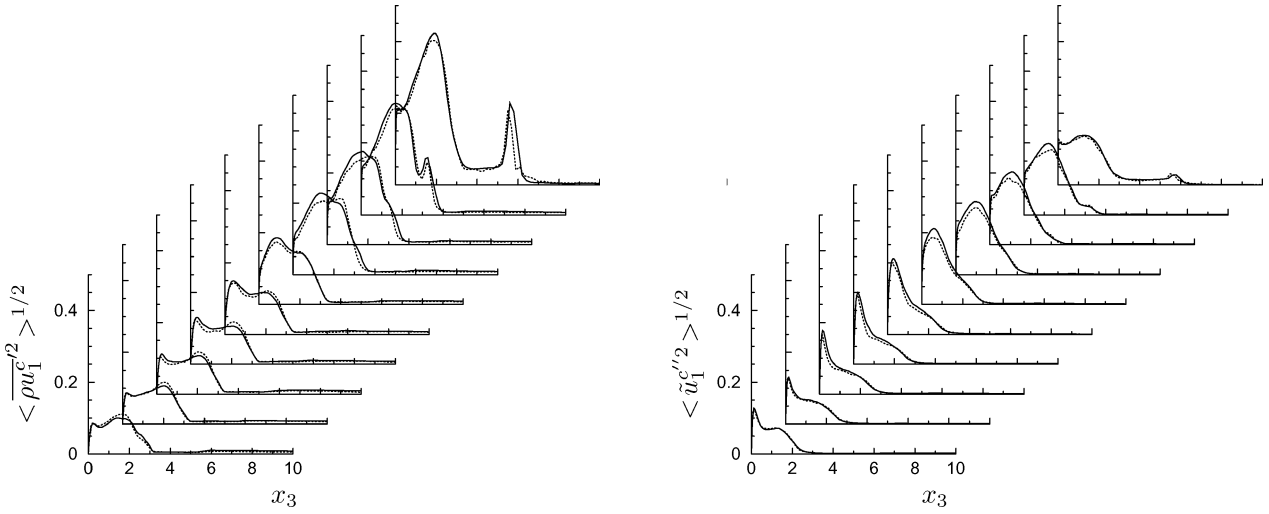

Fig. 13 Turbulent fluctuations: a) streamwise contravariant momentum rms fluctuations $\langle \overline{\rho u}_1^{c\prime 2} \rangle^{1/2}$ and b) streamwise contravariant Favre-averaged velocity fluctuations $\langle \tilde{u}_1^{c\prime\prime 2} \rangle^{1/2}$ at the streamwise stations 1–10 according to Fig. 6: ——, filtered DNS and . . . ., LES with ADM.

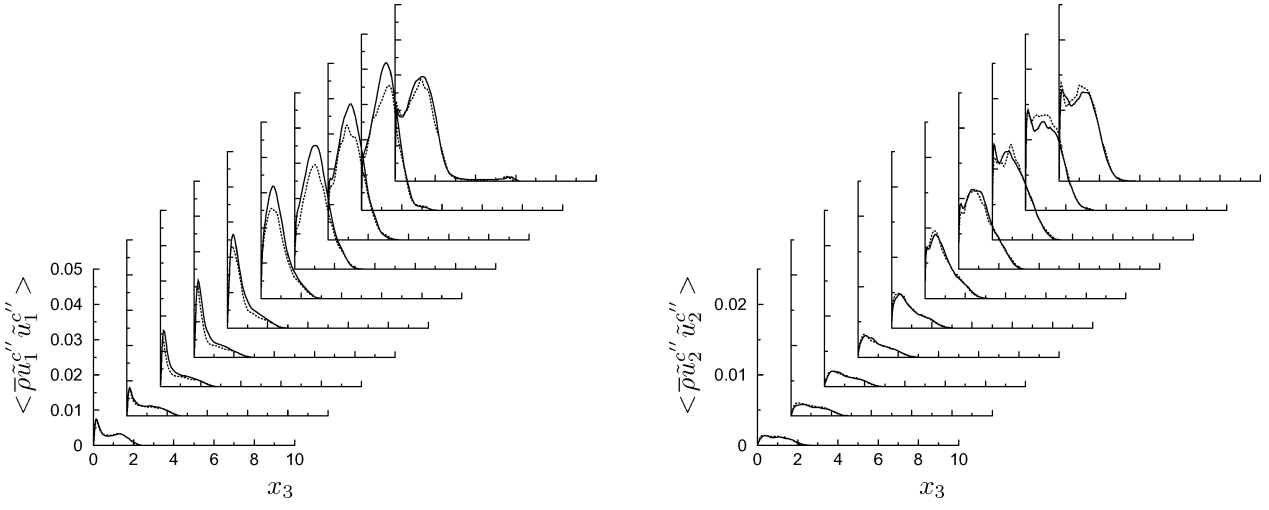

Fig. 14 Reynolds stress: a) $\langle \overline{\rho}\tilde{u}_1^{c\prime\prime}\tilde{u}_1^{c\prime\prime} \rangle$, b) $\langle \overline{\rho}\tilde{u}_2^{c\prime\prime}\tilde{u}_2^{c\prime\prime} \rangle$ at the streamwise stations 1–10 according to Fig. 6, where ——, filtered DNS and . . . . , LES with ADM.

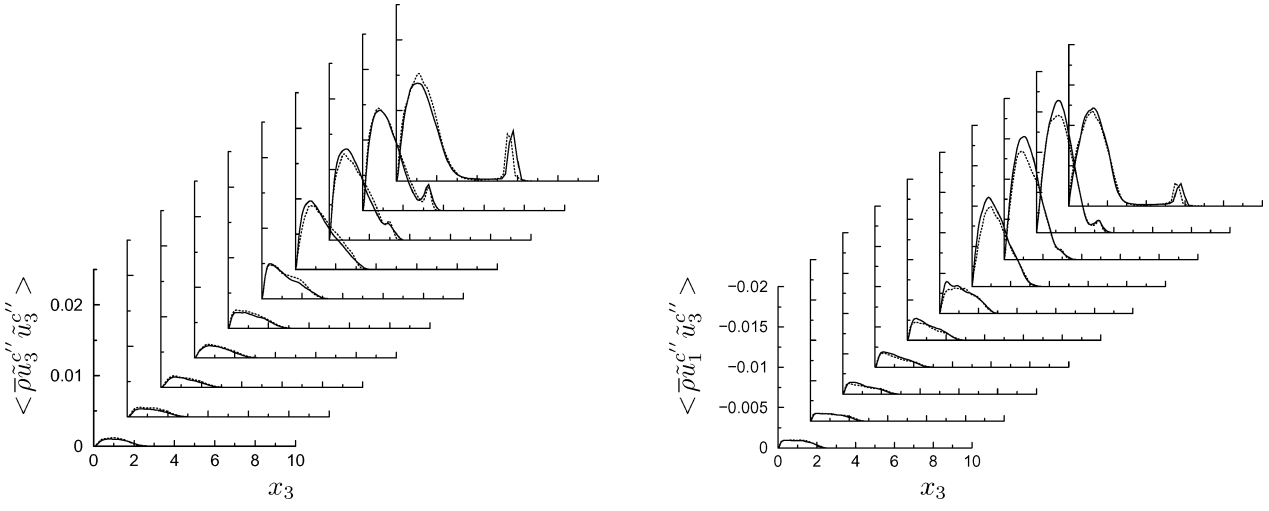

Fig. 15 Reynolds stress: a) $\langle \overline{\rho}\tilde{u}_3^{c\prime\prime}\tilde{u}_3^{c\prime\prime} \rangle$ and b) $\langle \overline{\rho}\tilde{u}_1^{c\prime\prime}\tilde{u}_3^{c\prime\prime} \rangle$ at the streamwise stations 1–10 according to Fig. 6, where ——, filtered DNS and . . . . , LES with ADM.

VI. Conclusions

The approximate deconvolution model was formulated to be used with a finite volume method. The convective terms are discretized in skew-symmetric form using a fourth-order centered scheme, whereas the viscous terms are computed using a second-order scheme on a shifted control volume. The subgrid-scale model is based on an approximate deconvolution of the filtered quantities by a truncated series expansion of the inverse filter. This approximation is used to compute the nonlinear terms in the Navier–Stokes equations, thus avoiding the need to compute subgrid-scale terms explicitly, except for adding a relaxation term. This relaxation term models the resolved-scale/nonrepresented-scale interaction by draining energy from the range of nonresolved represented scales $\omega_c < |\omega| \leq \omega_n$. No artificial numerical dissipation was used to damp the oscillations developing in the vicinity of the shock, but the deconvolution order N had to be lowered so as to maintain an accurate and stable computation. In the viscous-wall region, low deconvolution order was shown to be overdissipative so that the deconvolution order was increased in this region. Although in this work the deconvolution order was simply decreased with increasing wall distance, a more sophisticated procedure, for example, based on a pressure sensor, could be devised to automatically adjust the deconvolution order to the local flow regime. Validation of the implemented model was performed for the case of a supersonic compression ramp flow. A very good agreement between the filtered DNS[19] and the LES results was found for this complex flow problem, at a fraction of the cost (0.5% CPU time) of the DNS.

Appendix: Shock Tube

The shock tube problem[7,39] was considered to test the ability of ADM to represent accurately shock waves. The absence of turbulence allows for a clear evaluation of the energy dissipation mechanism across the discontinuity. For this configuration, a diaphragm at the location $x = 0.5$ initially separates a left (subscript l) and a right (subscript r) region of the flow, which have different densities and pressures. The two regions are in a constant state with pressure $p_l = 1$, $p_r = 0.1$, density $\rho_l = 1$, $\rho_r = 0.125$, and a zero velocity on each side of the diaphragm so that both fluids are initially at rest (Fig. A1; $t = 0$). At time $t = 0$ the diaphragm is broken. A shock wave, followed by a contact discontinuity, propagates then to the right and an expansion fan propagates to the left (Fig. A1; $t = 0.2$). To avoid the reflection of the shock and the expansion fan at the boundaries, we focus on the time span before any wave has reached the boundary of the computational domain. Furthermore, an inviscid fluid is assumed so that the one-dimensional Euler equations are considered. The temporal integration is carried out until $t = 0.2$ and the spatial mesh size is $\Delta x = 0.005$. For consistency with the compression ramp flow, the same fourth-order central scheme is used [Eq. (25)].

It is recalled that the deconvolution order N affects the approximate inverse quantity $\rho^\star = Q_N * \bar{\rho}$ and the relaxation term $-\chi(I - Q_N * G_1) * \bar{\rho}$ (see Sec. III). For further details on the effect of the deconvolution order, we refer to Sec V.A and display here only additional results obtained for the nonturbulent shock tube.

Figures A2a and A2b show the temporal evolution of the density for a deconvolution order of $N = 4$ and 1, respectively. The upper limit for the deconvolution order is dictated by stability reasons because the computation becomes unstable for $N = 5$, and the lower limit corresponds to the lowest deconvolution order used in the compression ramp simulation. The deconvolution order $N = 4$ damps only the high-wave-number range, and large-scale oscillations are still present in the flow as can be observed around the contact discontinuity and the shock in Fig. A2a. A much smoother solution is obtained when the deconvolution order is reduced to $N = 1$ (Fig. A2b), indicating that the large scales around the discontinuities have been filtered away. The deconvolution order also affects the relaxation parameter and relaxation term. The average value of the relaxation parameter χ is clearly smaller for the case $N = 1$ than for $N = 4$. This trend finds an explanation with the physical

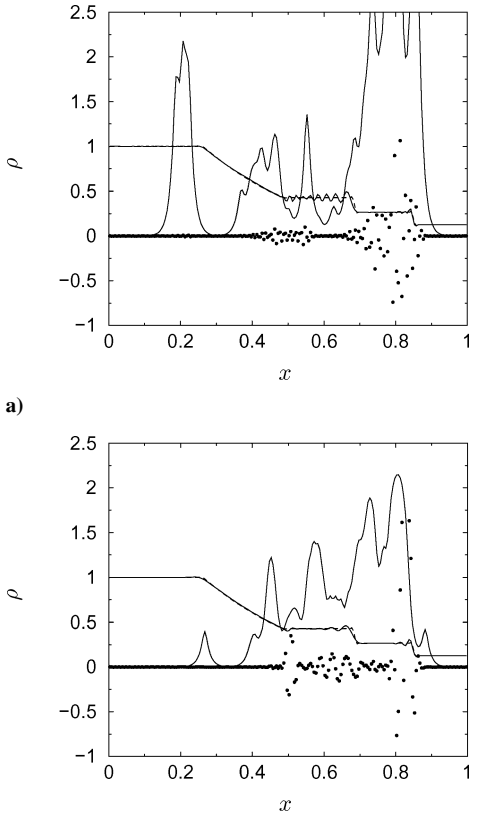

Fig. A2 Solution at time $t = 0.2$ for deconvolution order a) $N = 4$ and b) $N = 1$: ——, filtered density $\bar{\rho}$; ——, relaxation coefficient χ (value is divided by a factor of 10^2 for ease of representation on the graph); •, relaxation term $\chi(I - Q_N * G_1) * \bar{\rho}$ (value is multiplied by a factor 10^4 for ease of representation on the graph); and . . . . , exact filtered solution $\bar{\rho}_{\text{exact}}$.

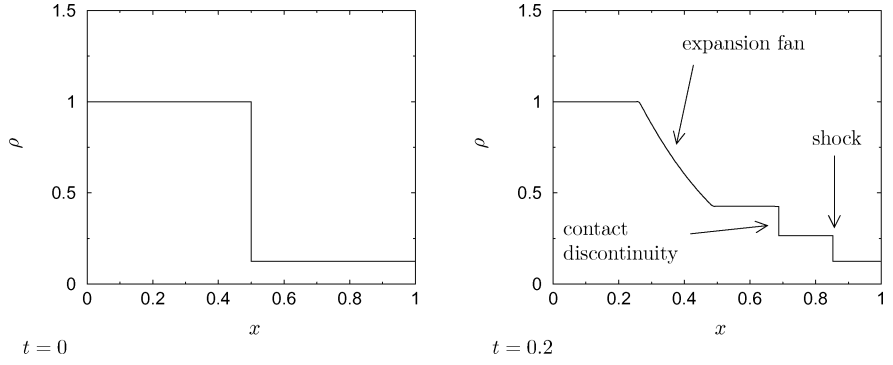

Fig. A1 Exact solution for the shock tube: ——, density ρ.

meaning of the relaxation parameter, which is the timescale with which energy is removed from the flow. The smaller energy removal wave-number range for $N = 4$ is thus compensated by a higher energy removal frequency. An inspection of the values of the relaxation term $-\chi(I - Q_N * G_1) * \bar{\rho}$ confirms this behavior. In average, the values of the relaxation term are lower for $N = 4$ than for $N = 1$, which can be interpreted as a low dissipation for the first case and an increased dissipation for the second case.

Similar investigations on the shock-capturing ability of ADM have recently been undertaken by Adams and Stolz.[15] They also varied the deconvolution order of the secondary filter G_2 present in the relaxation term. However, exact inversion (direct deconvolution model) of the solution needed for the nonlinear terms was performed in their case, that is, $\boldsymbol{U}^\star = \boldsymbol{U}$, and the relaxation parameter χ was kept constant. For test cases such as the slow-shock problem[40] and the Woodward–Colella blast wave,[41] they came to the same conclusions as found here, that is, that low-order secondary filters provide a better model of the dissipation mechanism across the shock.

Acknowledgments

Computations were performed on the NEC-SX-5 of the Swiss Center for Scientific Computing, in Manno. The authors thank Andreas Jocksch, Benjamin Rembold, and Steffen Stolz for stimulating discussions.

References

[1]Ackeret, J., Feldmann, F., and Rott, N., "Untersuchungen an Verdichtungsstössen und Grenzschichten in Schnell Bewegten Gasen," Mitteillungen Institut für Aerodynamik, TR, 10, ETH Zürich, Zurich, 1946.

[2]Dolling, D. S., "Fifty Years of Shock-Wave/Boundary-Layer Interaction Research: What Next?," *AIAA Journal*, Vol. 39, No. 8, 2001, pp. 1517–1531.

[3]Settles, G. S., Fitzpatrick, T. J., and Bogdonoff, S. M., "Detailed Study of Attached and Separated Compression Corner Flowfields in High Reynolds Number Supersonic Flow," *AIAA Journal*, Vol. 17, No. 6, 1979, pp. 579–585.

[4]Knight, D. D., and Degrez, G., "Shock Wave Boundary Layer Interactions in High Mach Number Flows. A Critical Survey of Current Numerical Predictions Capabilities," AGARD, Advisory Rept. 319, Vol. 2, Dec. 1998, pp. 1.1–1.35.

[5]Lax, P. D., and Wendroff, B., "Systems of Conservation Laws," *Communications on Pure and Applied Mathematics*, Vol. 13, No. 2, 1960, pp. 217–237.

[6]Godunov, S. K., "A Difference Method for Numerical Calculation of Discontinuous Solutions of the Equations of Hydrodynamics," *Mathematics Sbornik*, Vol. 47, No. 2, 1959, pp. 145–156.

[7]Leveque, R. J., *Finite Volume Methods for Hyperbolic Problems*, Cambridge Univ. Press, Cambridge, England,U.K., 2002.

[8]Garnier, E., Mossi, M., Sagaut, P., Comte, P., and Deville, M., "On the Use of Shock-Capturing Schemes for Large-Eddy Simulation," *Journal of Computational Physics*, Vol. 153, No. 2, 1999, pp. 273–311.

[9]Smagorinsky, J., "General Circulation Experiments with the Primitive Equations," *Monthly Weather Review*, Vol. 91, No. 3, 1963, pp. 99–164.

[10]Germano, M., Piomelli, U., Moin, P., and Cabot, W. H., "A Dynamic Subgrid-Scale Eddy Viscosity Model," *Physics of Fluids*, Vol. 3, No. 7, 1991, pp. 1760–1765.

[11]Boris, J. P., Grinstein, F. F., Oran, E. S., and Kolbe, R. L., "New Insights into Large-Eddy Simulation," *Fluid Dynamics Research*, Vol. 10, No. 4, 1992, pp. 199–228.

[12]Fureby, C., and Grinstein, F. F., "Monotonically Integrated Large Eddy Simulation of Free Shear Flows," *AIAA Journal*, Vol. 37, No. 5, 1999, pp. 544–556.

[13]Fureby, C., and Grinstein, F. F., "Large Eddy Simulation of High-Reynolds-Number Free and Wall-Bounded Flows," *Journal of Computational Physics*, Vol. 181, 2002, pp. 68–97.

[14]Stolz, S., Adams, N. A., and Kleiser, L., "An Approximate Deconvolution Model for Large-Eddy Simulations of Compressible Flows and Its Application to Shock-Turbulent-Boundary-Layer Interaction," *Physics of Fluids*, Vol. 13, No. 10, 2001, pp. 2985–3001.

[15]Adams, N. A., and Stolz, S., "A Subgrid-Scale Deconvolution Approach for Shock-Capturing," *Journal of Computational Physics*, Vol. 178, No. 2, 2002, pp. 391–426.

[16]Garnier, E., Sagaut, P., and Deville, M., "Large-Eddy Simulation of Shock/Boundary-Layer Interaction," *AIAA Journal*, Vol. 40, No. 10, 2002, pp. 1935–1944.

[17]Sagaut, P., *Large-Eddy Simulation for Incompressible Flows*, Springer-Verlag, Berlin, 2001, pp. 94, 95.

[18]Rizzetta, D. P., and Visbal, M. R., "Large-Eddy Simulation of Supersonic Compression Ramp Flow by High-Order Method," *AIAA Journal*, Vol. 39, No. 12, 2001, pp. 2283–2292.

[19]Adams, N. A., "Direct Simulation of the Turbulent Boundary Layer Along a Compression Ramp at $M = 3$ and $Re_\theta = 1685$," *Journal of Fluid Mechanics*, Vol. 420, 2000, pp. 47–83.

[20]Stolz, S., and Adams, N. A., "An Approximate Deconvolution Procedure for Large-Eddy Simulation," *Physics of Fluids*, Vol. 11, No. 7, 1999, pp. 1699–1701.

[21]Stolz, S., Adams, N. A., and Kleiser, L., "An Approximate Deconvolution Model for Large-Eddy Simulation with Application to Incompressible Wall-Bounded Flows," *Physics of Fluids*, Vol. 13, No. 4, 2001, pp. 997–1015.

[22]Rembold, B., Adams, N. A., and Kleiser, L., "Direct and Large-Eddy Simulation of Transitional Rectangular jet," *Direct and Large-Eddy Simulation IV*, edited by B. J. Geurts, R. Friedrich, and O. Métais, Kluwer, Dordrecht, The Netherlands, 2001, pp. 197–204.

[23]von Kaenel, R., Adams, N. A., Kleiser, L., and Vos, J. B., "The Approximate Deconvolution Method for Large-Eddy Simulation of Compressible Flows with Finite Volume Schemes," *Journal of Fluids Engineering*, Vol. 125, No. 2, 2003, pp. 375–381.

[24]von Kaenel, R., "Large-Eddy Simulation of Compressible Flows Using the Finite Volume Method," Ph.D. Dissertation, ETH 15255, Inst. of Fluid Dynamics, Zurich, Nov. 2003, URL: http://e-collection.ethbib.ethz.ch.

[25]Vos, J. B., Rizzi, A. W., Corjon, A., Chaput, E., and Soinne, E., "Recent Advances in Aerodynamics Inside the NSMB (Navier–Stokes Multi-Block) Consortium," AIAA Paper 98-0225, Jan. 1998.

[26]Stolz, S., Adams, N. A., and Kleiser, L., "LES of Shock-Boundary Layer Interaction with the Approximate Deconvolution Model," *Proceedings of the 8th European Turbulence Conference*, edited by C. Dopazo, International Center for Numerical Methods in Engineering, Barcelona, 2000, pp. 715–718.

[27]Stolz, S., "Large-Eddy Simulation of Complex Shear Flows Using an Approximate Deconvolution Model," Ph.D. Dissertation, ETH No. 13861, Inst. of Fluid Dynamics, Zurich, 2000; also Fortschritt-Bericht VDI Reihe 7, No. 403.

[28]Adams, N. A., "The Role of Deconvolution and Numerical Discretization in Subgrid-Scale Modeling," *Direct and Large-Eddy Simulation IV*, edited by B. J. Geurts, R. Friedrich, and O. Métais, Kluwer, Dordrecht, The Netherlands, 2001, pp. 311–320.

[29]Lesieur, M., and Métais, O., "New Trends in Large-Eddy Simulations of Turbulence," *Annual Review of Fluid Mechanics*, Vol. 28, 1996, pp. 45–82.

[30]Batchelor, G. K., *The Theory of Homogenous Turbulence*, Cambridge Univ. Press, Cambridge, England, U.K., 1953.

[31]Lele, S. K., "Compact Finite Difference Schemes with Spectral-Like Resolution," *Journal of Computational Physics*, Vol. 103, No. 1, 1992, pp. 16–42.

[32]Domaradzki, J. A., and Radhakrishnan, S., "Subgrid-Scale Modeling of Turbulent Convection Using Truncated Navier-Stokes Dynamics," *Journal of Fluids Engineering*, Vol. 124, No. 4, 2002, pp. 823–828.

[33]Visbal, M. R., Morgan, P. E., and Rizzetta, D. P., "An Implicit LES Approach Based on High-Order Compact Differencing and Filtering Schemes," AIAA Paper 2003-4098, June 2003.

[34]Hirsch, Ch., *Numerical Computation of Internal and External Flows, Vol. 2, Computational Methods for Inviscid and Viscous Flows*, Wiley, Chichester, England, U.K., 1990.

[35]Blaisdell, G. A., Spyropoulos, E. T., and Qin, J. H., "The Effect of the Formulation of Nonlinear Terms on Aliasing Errors in Spectral Methods," *Applied Numerical Mathematics*, Vol. 21, No. 3, 1996, pp. 207–219.

[36]Ducros, F., Laporte, F., Soulères, T., Guinot, V., Moinat, P., and Caruelle, B., "High-Order Fluxes for Conservative Skew-Symmetric-Like Schemes in Structured Meshes: Application to Compressible Flows," *Journal of Computational Physics*, Vol. 161, No. 1, 2000, pp. 114–139.

[37]Peyret, R., and Taylor, T. D., *Computational Methods for Fluid Flows*, Springer-Verlag, New York, 1983.

[38]Jameson, A., Schmidt, W., and Turkel, E., "Numerical Solution of the Euler Equations by Finite Volume Methods Using Runge–Kutta Time Stepping Schemes," AIAA Paper 81-1259, July 1981.

[39]Sod, G. A., "A Survey of Several Finite Difference Methods for Systems of Nonlinear Hyperbolic Conservation Laws," *Journal of Computational Physics*, Vol. 27, 1978, pp. 1–31.

[40]Roberts, Th. W., "The Behavior of Flux Difference Splitting Schemes near Slowly Moving Shock Waves," *Journal of Computational Physics*, Vol. 90, No. 1, 1990, pp. 141–160.

[41]Woodward, P., and Colella, P., "The Numerical Simulation of Two-Dimensional Flow with Strong Shocks," *Journal of Computational Physics*, Vol. 54, No. 1, 1984, pp. 115–173.

P. Givi
Associate Editor